

Communication

Estimation of spin-echo relaxation time

F. Golub^a, L.C. Potter^{a,b}, J.N. Ash^a, A. Blank^c, R. Ahmad^{a,b,*}^a Department of Electrical and Computer Engineering, The Ohio State University, Columbus, OH 43210, USA^b Davis Heart and Lung Research Institute, The Ohio State University, Columbus, OH 43210, USA^c Schulich Faculty of Chemistry, Technion – Israel Institute of Technology, Haifa 32000, Israel

ARTICLE INFO

Article history:

Received 21 July 2013

Revised 5 September 2013

Available online 19 September 2013

Keywords:

EPR

NMR

Hahn echo

Oximetry

Efficient estimator

Cramér-Rao lower bound

Singular value decomposition

ABSTRACT

In spin-echo-based EPR oximetry, traditional methods to estimate the T_2 relaxation time, which encodes the oxygen concentration of the sample, include fitting an exponential to the peaks or the integrated areas of multiple noisy echoes. These methods are suboptimal and result in a loss of estimation precision for a given acquisition time. Here, we present the maximum likelihood estimate (MLE) of T_2 from spin-echo data. The MLE provides, for the data considered, approximately 3-fold time savings over echo-integration and more than 40-fold time savings over peak-picking. A one-dimensional line search results in simple computation of the MLE. It is observed that, perhaps counter-intuitively, prior knowledge of the lineshape does not yield additional reduction of estimation error variance at practical noise levels. The result also illuminates the near optimal performance of T_2 estimation via principal components calculated by a singular value decomposition. The proposed method is illustrated by application to simulated and experimental EPR data.

© 2013 Elsevier Inc. All rights reserved.

1. Introduction

Electron paramagnetic resonance (EPR) is a spectroscopic method capable of detecting and quantifying free radicals. Over the past several decades, EPR has found numerous applications in biology, chemistry, physics, and medicine [1]. Among in vivo applications of EPR, oximetry has been arguably the most active topic of research, with emphasis on quantitative assessment of tumor hypoxia [2,3].

Continuous wave (CW) EPR and pulsed EPR are competing yet often complementary modes of data acquisition. At present, CW EPR remains the most widespread technique for in vivo oximetry [4] because of its simple equipment design and ability to utilize a wide variety of oxygen sensitive spin probes. However, the data acquisition in CW EPR is generally slow, resulting in long acquisition times. One way to accelerate data acquisition is to use pulsed EPR methods. With recent technological advances and the development of EPR oximetry probes with narrow linewidth, pulsed EPR oximetry has become an attractive option, especially for studying tumor hypoxia [5].

The early pulsed EPR oximetry experiments measured the decaying signal, called free induction decay (FID), after the application of a $\pi/2$ pulse [6]. To calculate the transverse relaxation time, the measured FID is fitted with an exponential. For FID-based

imaging, one-dimensional projections are obtained by the Fourier transformation of the FID signal collected in the presence of frequency encoding gradients [7]. The image is generally obtained by filtered backprojection of the measured projection data. The dead-time of EPR spectrometers irreversibly distorts the leading portion of the FID signal, decreasing the efficiency, especially for probes with short relaxation times. This limitation of FID-based EPR oximetry is overcome by the use of spin-echo (SE) acquisition, which has been used in both spectroscopic and imaging modes [5]. Another alternative approach to EPR oximetric imaging is single point imaging (SPI)—a pure phase encoding technique—which offers superior spatial resolution albeit at the cost of longer acquisitions [8]. These pulsed EPR methods have been summarized in a review article by Subramanian et al. [9].

The present work pertains to SE-based spectroscopy with application to EPR oximetry. The SE-based EPR oximetry allows direct measurement of the T_2 relaxation time, which can be readily converted to the homogeneous broadening component of the EPR lineshape. Since the homogeneous broadening is proportional to the oxygen concentration, broadening can thus be used to estimate oxygen concentration via a precomputed calibration curve.

In SE-EPR, data are generally collected using the conventional $\pi/2 - \tau - \pi - \tau$ echo pulse sequence [10]. Since the echo amplitude decays with $\exp\{-2\tau/T_2\}$, collecting and processing multiple echoes with different τ values enables estimation of T_2 . The traditional methods of processing SE-EPR data include fitting an exponential to echo peaks (peak-picking) or echo areas (echo-integration). The peak-picking method is inefficient because it only

* Corresponding author. Address: 420 W 12th Ave., Suite 126A, Columbus, OH 43210, USA. Fax: +1 614 292 8454.

E-mail address: ahmad.46@osu.edu (R. Ahmad).

uses one data point from each echo, and echo-integration is likewise inefficient because it does not distinguish between high-SNR and low-SNR samples in an echo.

Here, we present a maximum likelihood estimator of the T_2 relaxation time. The estimator achieves the Cramér-Rao lower bound (CRLB) on estimation error variance at experimentally relevant noise levels. The precision of the estimate allows for approximately 3 times acceleration of data acquisition over the echo-integration method, and over 40 times acceleration versus peak-peaking. Interestingly, knowledge of the lineshape does not provide improvement in precision of T_2 estimates.

2. Theory

The purpose of data acquisition and processing is to produce an estimate of the T_2 relaxation time. In this section, we first review the peak-picking and echo-integration estimators. Then, we present and analyze the maximum likelihood estimator.

2.1. Peak-picking and echo integration

In the peak-picking method (e.g., [7,11]), the estimate of T_2 is determined by a least-squares fit of an exponential to high-amplitude samples taken from N measured echoes:

$$\hat{T}_{2,pp} = \operatorname{argmin}_{T_2, T_2, a} \sum_{k=1}^N |s_k - a \exp(-2\tau_k/T_2)|^2, \quad (1)$$

where s_k is the sample from the k th echo taken at a fixed position common to all echoes, a is an unknown scaling, and $2\tau_k$ is the echo time for the k th pulse. For complex-valued spectra, s_k and a in (1) are complex-valued numbers.

In the echo-integration method (e.g., [11,12]), each echo is integrated before fitting a decaying exponential. Thus, the estimated relaxation time is

$$\hat{T}_{2,ei} = \operatorname{argmin}_{T_2, T_2, a} \sum_{k=1}^N |\bar{y}_k - a \exp(-2\tau_k/T_2)|^2, \quad (2)$$

where, for real-valued spectra, \bar{y}_k is the sum of the M equi-spaced sampled values for the k th echo. For complex-valued spectra, a is complex-valued, and we take \bar{y}_k to be the complex-valued coefficient of the most energetic harmonic in the discrete Fourier series expansion of y_k .

2.2. Maximum likelihood estimator

We derive a simple expression for the MLE of the T_2 relaxation time and demonstrate that no assumption is required on the lineshape. Further, the approach accommodates different amounts of averaging, and hence effective noise power, at each echo. Consider a data matrix formed by concatenating each measured echo into a column of an $M \times N$ matrix, Y . An exponential decay of echoes can be written

$$Y = afb^H(T_2) + G, \quad (3)$$

where $Y = [y_1, y_2, \dots, y_N]$ is an $M \times N$ array, a is an unknown global scaling, f is a length- M list of samples of the echo shape with unit norm $\|f\|_2 = 1$, and $b(T_2) = [\exp\{-2\tau_1/T_2\}, \dots, \exp\{-2\tau_N/T_2\}]^H$, is the exponential decay at N echo times. Here and below, superscript $(\cdot)^H$ denotes the conjugate transpose. The measurement noise matrix G is an $M \times N$ array of independent Gaussian random variables with zero mean and variance $w_k \sigma^2$ in column k (variance $w_k \sigma^2/2$ in both real and imaginary parts, in the case of complex-valued spectra). For example, with identical instrument noise at each echo, we have simply $w_k = 1/R_k$, where R_k is the number of averages used to

form the k^{th} echo. Note that b is real-valued, whereas a , f , and G can be either real or complex-valued depending on the measured data Y .

The scale factor, a , the echo shape, f , the noise factor σ^2 , and the relaxation time, T_2 , are all unknown; from Y we seek the maximum-likelihood estimate of T_2 . The likelihood function is

$$\begin{aligned} \mathcal{L}(T_2) &= (2\pi\sigma^2)^{-MN/2} |W|^{-M/2} \\ &\times \exp \left\{ -\frac{1}{2\sigma^2} \| (Y - afb^H(T_2)) W^{-1/2} \|_F^2 \right\}, \end{aligned} \quad (4)$$

where $W = \operatorname{diag}\{w_1, \dots, w_N\}$ and $\|\cdot\|_F$ denotes the Frobenius norm (i.e., square root of sum of squares of entries in the matrix). Hence, by the monotonicity of the logarithm, the ML estimate is

$$\hat{T}_{2,ml} = \operatorname{argmin}_{T_2, a, T_2, f} \| (Y - afb^H(T_2)) W^{-1/2} \|_F^2. \quad (5)$$

The N -by- N matrix $W^{-1/2}$ may be interpreted as a whitening filter. As shown in Appendix A, the optimizing value of T_2 in (5) is

$$\hat{T}_{2,ml} = \operatorname{argmax}_{T_2} \frac{b^H(T_2) W^{-1} Y^H Y W^{-1} b(T_2)}{b^H(T_2) W^{-1} b(T_2)}. \quad (6)$$

Because b is structured by the parameter T_2 , a one-dimensional line search is required to optimize (6) and obtain both the ML estimate $\hat{T}_{2,ml}$ and the associated vector $b(\hat{T}_{2,ml})$. Similarly, for the case in which the echo shape is assumed to be known, the MLE becomes

$$\hat{T}_{2,ml-f} = \operatorname{argmax}_{T_2} \frac{b^H(T_2) W^{-1} Y^H f^H Y W^{-1} b(T_2)}{b^H(T_2) W^{-1} b(T_2)}, \quad (7)$$

where f is the known echo shape with unit norm. A brief computer code for (6) and (7) in the Matlab language (Mathworks, Natick, MA) is available at Matlab Central File Exchange [13].

2.3. Singular value decomposition

Under noiseless ideal conditions, Y is a rank-one matrix, which motivated us to explore estimation of T_2 from the singular value decomposition (SVD) [14]. The SVD provides the following matrix decomposition,

$$Y = \sum_{r=1}^N \sigma_r u_r v_r^H, \quad \sigma_1 \geq \sigma_2 \geq \dots \geq \sigma_N \geq 0, \quad (8)$$

where, for M samples per each of $N < M$ echoes, $\{u_1, \dots, u_N\}$ are orthonormal vectors of length M , and $\{v_1, \dots, v_N\}$ are orthonormal vectors of length N . Under the assumption that the noiseless echo has the same shape for each delay time $2\tau_k$, then the noiseless data matrix must be a rank-one matrix. Accordingly, u_1 is the normalized echo shape, and the N values in v_1 are samples of the decay curve, in the noiseless case.

If b were unstructured, rather than an exponential decay, then in noise the likelihood maximizing value for b (up to scale) in (6) would be given by the eigenvector corresponding to the largest eigenvalue of $Y^H Y$. Note, the latter is equivalent to the principal right singular vector, v_1 , of Y .

It is interesting to consider how the solution to (6) compares to an SVD-based estimator of T_2 ; in Appendix B, we establish the equality

$$\begin{aligned} \hat{T}_{2,svd} &= \operatorname{argmin}_{T_2, T_2, a} \sum_{k=1}^N \| Y_k - au_1 \exp(-2\tau_k/T_2) \|^2 \\ &= \operatorname{argmax}_{T_2} \frac{b^H(T_2) v_1 v_1^H b(T_2)}{b^H(T_2) b(T_2)}. \end{aligned} \quad (9)$$

Hence, we find that when Y is truly rank-one (that is, in the noiseless case), the MLE and SVD-based estimators coincide:

$\widehat{T}_{2,svd} = \widehat{T}_{2,ml}$. In noise, the SVD estimator, while suboptimal and computationally more expensive than the MLE, can offer near-optimal performance for the case of equal noise variance in each recorded echo.

3. Materials and methods

3.1. Simulation

For a controlled numerical experiment, EPR spin echo data were simulated in Matlab (Mathworks, Natick, MA) using random additive noise. The signal was modeled using real-valued Gaussian echoes, yielding

$$Y_0(t, k) = a \exp\{-(t - m)^2 / \nu\} \exp\{-2\tau_k/T_2\}, \\ t = 1, \dots, 256, \quad k = 1, \dots, 7, \quad (10)$$

where $m = 100$, $\nu = 1245$, and $T_2 = 418$ ns; 256 uniformly-spaced time samples were generated at a 1 ns spacing. The parameters were selected to mimic experimental data from activated charcoal (data not presented) [15].

The seven echo times, 2τ , were 400 to 880 ns in uniform increments of 80 ns. The seven simulated echoes were used to form a noiseless 256×7 data array, Y_0 . For 10,000 Monte Carlo trials, pseudo-random zero-mean Gaussian noise of variance σ^2 was added to Y_0 to yield a signal-to-noise ratio (SNR) from -10 dB to 30 dB, in increments of 2 dB; accordingly, simulated noise variances, σ^2 , were given by

$$\text{SNR(dB)} = 10 \log_{10} \frac{\|Y_0\|_F^2}{MN\sigma^2}. \quad (11)$$

Additionally, the Cramér-Rao lower bounds [16,17] were computed for the estimation error variance on signal models corresponding to peak-picking, echo-integration, and the non-parametric signal model of (3). The CRLB gives a lower bound on the variance of any unbiased estimator; a MLE is asymptotically a statistically efficient estimator, and thus achieves this bound at sufficiently high signal to noise ratio (SNR). We note that the CRLB, which is essentially a high-SNR analysis, yields identical lower bounds for three cases: unknown echo shape, parametric echo shape with unknown parameters (e.g., Gaussian pulse with unknown width and shift), and known echo shape with unknown amplitude.

3.2. Experimental data

Finland D36 trityl [18] under anoxic conditions at 1 mM concentration was used to collect spin-echo data on a home made wide band pulsed EPR spectrometer [19] operated at 9.5 GHz. Other parameters used were: Hahn echo sequence with 35 ns $\pi/2$ pulse and 80 ns π pulse; 8-step phase cycle (CYCLOPS and \pm on the first pulse); time domain sampling rate of 500 MHz; and repetition rate of 20 kHz. Sixteen echoes were collected with 2τ ranging from 1600 ns to 10,600 ns, with a constant increment of 600 ns. Two datasets, one high SNR (25.8 dB) for building the ground truth and one at low SNR (1 dB) for validation, were collected back to back. For the high SNR dataset, 24,000 averages were used for every echo, while only 80 averages per echo were used for the low SNR dataset. The low SNR acquisition was repeated 18 times under identical conditions.

4. Results

4.1. Simulation

Fig. 1(a) displays the standard deviation of T_2 estimation error for five estimation methods: peak-picking, echo-integration, SVD,

MLE with known lineshape, and MLE with unknown linshape. The solid lines depict the optimal performance bounds given by the square root of the CRLBs, and circles show simulated results computed from the 10,000 random noise realizations at each SNR. The estimation bias is the mean of the estimation errors and is given in Fig. 1(b). Five observations are drawn from the simulated noise experiments in Fig. 1. First, the standard errors for the peak-picking and echo-integration, in ratio to the MLE, are $\sqrt{44.2}$ and $\sqrt{2.89}$, respectively. Thus, the simple MLE post-processing can achieve a desired estimation precision with 2.89 times and 44.2 times shorter acquisition compared to echo-integration and peak-picking, respectively. Second, the MLE provides low bias estimates at lower SNR than is achieved with either peak-picking or echo-integration. Third, for SNR values above 0 dB, the estimator error in both bias and standard deviation is essentially identical for maximum likelihood estimation with and without presumed knowledge of the echo shape; thus, one should choose to make inference of T_2 agnostic to echo shape. Fourth, the SVD-based estimator yields bias and variance essentially identical to the MLE with unknown lineshape, as predicted in (26). Fifth, the CRLB provides an accurate analytical prediction of estimation precision for experimentally relevant SNR values—in this case, above 10 dB SNR for the peak-picking estimator and above 0 dB for the other four estimators considered.

4.2. Experimental data

All four methods—peak-picking, echo-integration, SVD, and MLE (with unknown lineshape)—generated similar estimates of T_2 from the high SNR dataset: $\widehat{T}_{2,p} = 6305$ ns, $\widehat{T}_{2,ei} = 6504$ ns, $\widehat{T}_{2,svd} = 6500$ ns, and $\widehat{T}_{2,ml} = 6502$ ns. The estimate based on echo integration was used as the ground truth. Three of the sixteen complex echoes from the high SNR dataset and from one of the low SNR datasets are shown in Figs. 2 and 3, respectively.

We evaluated the performance of the four estimators by computing T_2 estimates for each of the 18 low SNR acquisitions. The distribution of these estimates is reported in Fig. 4. Compared to the standard deviation of 239.8 ns for $\widehat{T}_{2,ml}$, the standard deviations in $\widehat{T}_{2,pp}$, $\widehat{T}_{2,ei}$, and $\widehat{T}_{2,svd}$ were observed to be 1912 ns, 447.9 ns, and 241.1 ns, respectively. Assuming $\text{std}(\widehat{T}_2) \propto 1/\sqrt{t}$, with t being the acquisition time, the time savings offered by MLE over peak-picking and echo-integration were 63.6-fold and 3.49-fold, respectively. Also, compared to the traditional estimators, the bias was smaller for $\widehat{T}_{2,ml}$ and $\widehat{T}_{2,svd}$.

5. Discussion

T_2 estimation based on traditional peak-picking or echo-integration is suboptimal. In a typical spin-echo experiment, the samples along an echo have varying SNR; the peak has higher SNR compared to the other samples in the echo. In peak-picking, most of the collected data are disregarded, resulting in an efficiency loss. Although the echo-integration method utilizes all the data samples, it does not take SNR variations into account; high and low SNR samples are averaged together, resulting in a suboptimal performance.

In general, the performances of peak-picking and echo-integration, relative to the MLE, depend on the shape of the echo, making it difficult to project the exact time-savings offered by MLE for all possible experimental setups. For the data considered, approximately 3-fold time savings over echo-integration and more than 40-fold time savings over peak-picking were observed.

Another potential advantage of the MLE and the related statistical sensitivity analysis is their use to optimize data collection to provide the best precision for a given acquisition time. Previously,

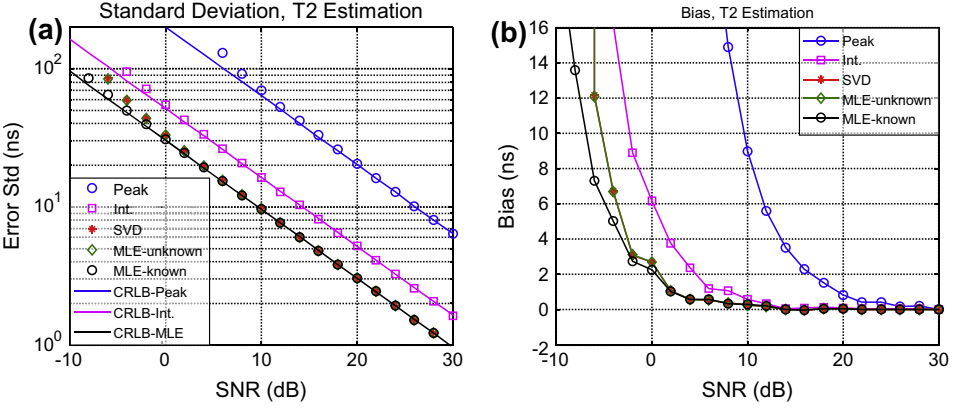


Fig. 1. Simulation results for 10,000 trials of additive Gaussian noise. Standard deviation of T_2 estimation error (a) and estimation bias (b) are shown. The solid lines in (a) depict optimal bounds given by the square root of CRLBs. Here, “Peak” and “Int.” indicate peak-picking and echo-integration, respectively, and “MLE-known” and “MLE-unknown” represent MLE for known and unknown lineshapes, respectively.

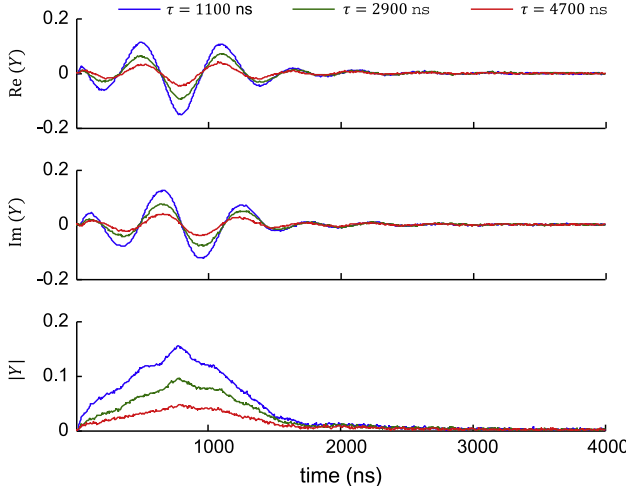


Fig. 2. Three of the sixteen echoes from the high SNR experimental data are shown. From top to bottom are the real, imaginary, and absolute values of the measured echo data.

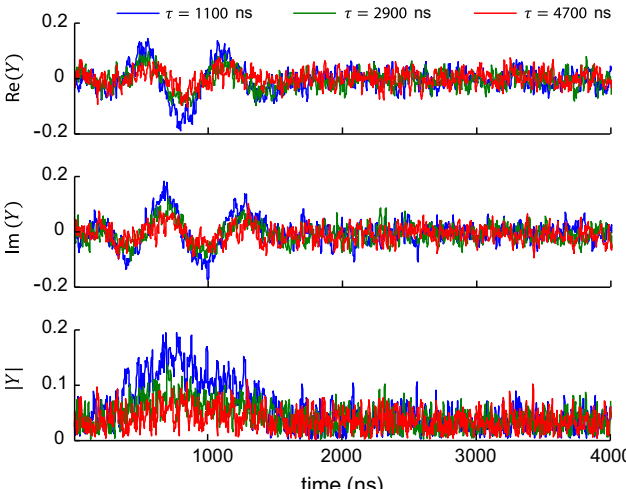


Fig. 3. Three of the sixteen echoes from the low SNR experimental data are shown. From top to bottom are the real, imaginary, and absolute values of the measured echo data.

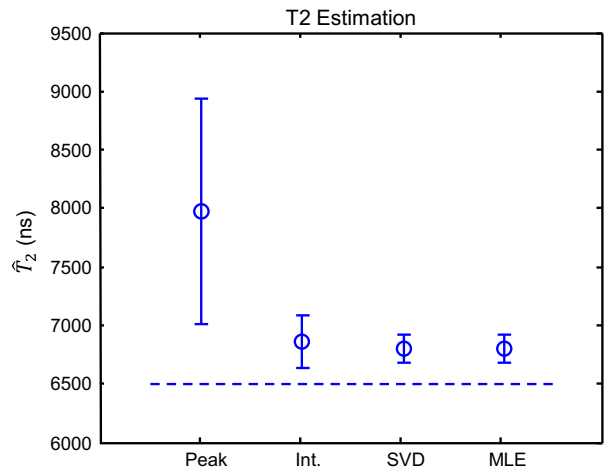


Fig. 4. Performance of four different estimators for the experimental data with low SNR. The horizontal dashed-line represents the ground truth based on $T_{2,ei}$ from high SNR dataset. The symbol “o” represents the mean value of estimated T_2 and the errorbars represents $\pm \frac{1}{2}\text{std}$. Again, “Peak” and “Int.” indicate peak-picking and echo-integration, respectively.

we have employed similar analysis to optimize data collection for CW EPR [20]. In addition, such analysis can also be used to develop a relationship between ambient SNR and T_2 (or oxygen) measurement precision, albeit only for a given set of experimental parameters and probe characteristics.

The proposed estimator is equally applicable to real or complex-valued echoes, and also allows unequal numbers of averages (SNR) across the echoes. Computationally, the proposed MLE is fast. For the experimental dataset, the average computation times for peak-picking, echo-integration, SVD, and MLE were approximately 70 ms, 50 ms, 125 ms, and 25 ms, respectively. Although the relative values of these computation times may vary based on the employed optimization routines, the reliance on one-dimensional line search will ensure that the MLE computation burden compares favorably against existing methods.

Interestingly, the MLE of T_2 is asymptotically agnostic to the shape of the echo, i.e., knowing the parametric form of the echo or knowing the echo explicitly does not change the CRLB (derivation not shown). The Monte Carlo simulation (Fig. 1) agrees with the theoretical prediction; and, at very low SNR (below

0 dB) the explicit knowledge of echo shape offers a modest improvement.

Although it is not the primary focus of this work, the MLE framework detailed in [Appendix A](#) enables estimating the echo shape as well. In fact, after the MLE of T_2 has been computed via line search, the estimation of the underlying echo shape has a closed-form solution (Eq. [\(14\)](#), with b constructed from $\hat{T}_{2,ml}$). Note that the work presented here is equally applicable to T_1 -based EPR oximetry [\[21\]](#).

In the field of NMR or MRI relaxometry, several data processing techniques have been proposed to estimate T_2 from spin-echo data. Although they bear a resemblance to the proposed MLE method, the estimation of T_2 for almost all those techniques relies on fitting a series of measured data samples with a single or multiple exponential functions [\[22–24\]](#). The proposed method offers a departure from the previous work. Here, we process the entire echo and exploit the redundancy of spin-echo data. Also, our application of SVD is different. Previously, SVD has been used to denoise spin-echo based MRI images [\[25\]](#), while we have used SVD as a means to jointly process data for T_2 estimation.

In addition to being a statistically principled estimation technique, the proposed MLE can seamlessly accommodate unequal noise variance across echoes, whereas SVD cannot. However, application of the MLE method is limited to spin-echo spectroscopy and cannot be readily extended to imaging. In contrast, the SVD concepts presented here can be extended to imaging applications. In SE-based imaging, a series of two- or three-dimensional images with different delays τ between $\pi/2$ and π pulses is acquired, and the intensity decay at every pixel or voxel is fitted to an exponential function to generate a T_2 map. We can rearrange the imaging data into a 2D matrix Y , such that the pixel intensities are along the column-direction and pixel-wise relaxation rates are along the row-direction. Since the relaxation rates vary spatially, the matrix Y has rank larger than 1. In this case, however, SVD can still be applied to denoise images, with some appropriate choice of truncation of singular values in [\(8\)](#). Similar denoising approaches have been previously used [\[26,25,27\]](#). Finally, the local T_2 values can be determined by pixel-wise fitting of the denoised image with an exponential function. This approach can potentially overcome the “missing voxel” issue encountered in SE-EPR imaging where extremely poor SNR at a given pixel or voxel results in a meaningless exponential fit [\[5\]](#).

6. Conclusion

The proposed maximum likelihood estimate of the T_2 relaxation time provides significant reduction in standard error—and hence acquisition time—versus the peak-picking and echo-integration techniques commonly used in the literature. Further, the MLE does not benefit from prior knowledge of the true lineshape at practical noise levels. For the simulated and experimental data presented, a time savings of 2.89:1 and 3.49:1, respectively, were observed versus echo-integration, with much larger savings versus peak-picking. Thus, simple post-processing can provide low-variance estimates of T_2 relaxation times using accelerated acquisition and without prior knowledge of a functional form for the spin echo.

Appendix A. MLE derivation

We proceed by first obtaining a closed-form expression for $x = af$ for a given T_2 . Let \tilde{y} denote a stacking of the columns of $YW^{-1/2}$, then

$$\|(Y - xb^H(T_2))W^{-1/2}\|_F^2 = \left\| \tilde{y} - \begin{bmatrix} b_1(T_2)\sqrt{1/w_1}I_M \\ b_2(T_2)\sqrt{1/w_2}I_M \\ \vdots \\ b_N(T_2)\sqrt{1/w_N}I_M \end{bmatrix} x \right\|_F^2, \quad (12)$$

where I_M is the M -by- M identity matrix. Hence, given T_2 , the value of $x = af$ minimizing [\(12\)](#) is

$$\hat{x}(T_2) = (Q^H(T_2)Q(T_2))^{-1}Q^H(T_2)\tilde{y}. \quad (13)$$

Omitting the T_2 -dependence of $b(T_2)$ for clarity and simplifying [\(13\)](#), we obtain

$$\begin{aligned} \hat{x}(T_2) &= \left(b_1^2 w_1^{-1} I_M + b_2^2 w_2^{-1} I_M + \cdots + b_N^2 w_N^{-1} I_M \right)^{-1} \\ &\quad \times [b_1 \sqrt{1/w_1} I_M, b_2 \sqrt{1/w_2} I_M, \dots, b_N \sqrt{1/w_N} I_M] \tilde{y} \\ &= \frac{[b_1 \sqrt{1/w_1} I_M, b_2 \sqrt{1/w_2} I_M, \dots, b_N \sqrt{1/w_N} I_M] \tilde{y}}{\sum_k b_k^2 w_k^{-1}} \\ &= \frac{YW^{-1}b}{\|W^{-1/2}b\|^2}. \end{aligned} \quad (14)$$

The objective [\(5\)](#) reduces to

$$\begin{aligned} \hat{T}_{2,ml} &= \arg \min_{T_2} \|(Y - x(T_2)b^H(T_2))W^{-1/2}\|_F^2 \\ &= \arg \min_{T_2} \left\| YW^{-1/2} - \frac{YW^{-1}b(T_2)b^H(T_2)W^{-1/2}}{\|W^{-1/2}b(T_2)\|^2} \right\|_F^2. \end{aligned} \quad (15)$$

The later has a number of different forms which lead us to a simplified expression that is useful for both computation and insight. Let $Y = YW^{-1/2}$ and $B = (W^{-1/2}bb^HW^{-1/2})/(b^HW^{-1}b)$, then we have

$$\hat{T}_{2,ml} = \arg \min_{T_2} \|\tilde{Y}(I - \tilde{B})\|_F^2 \quad (16)$$

$$= \arg \min_{T_2} \text{tr}(\tilde{Y}(I - \tilde{B})(I - \tilde{B})^H \tilde{Y}^H) \quad (17)$$

$$= \arg \min_{T_2} \text{tr}(\tilde{Y}(I - \tilde{B} - \tilde{B} + \tilde{B}^2)\tilde{Y}^H) \quad (18)$$

$$= \arg \min_{T_2} \text{tr}(\tilde{Y}\tilde{Y}^H - \tilde{Y}\tilde{B}\tilde{Y}^H) \quad (19)$$

$$= \arg \max_{T_2} \text{tr}(\tilde{Y}\tilde{B}\tilde{Y}^H) \quad (20)$$

$$= \arg \max_{T_2} \text{tr}\left(\frac{YW^{-1}bb^HW^{-1}Y^H}{b^HW^{-1}b}\right). \quad (21)$$

Finally, explicitly denoting the T_2 dependence of b , we have

$$\hat{T}_{2,ml} = \arg \max_{T_2} \frac{b^H(T_2)W^{-1}Y^HYW^{-1}b(T_2)}{b^H(T_2)W^{-1}b(T_2)} \quad (22)$$

At [\(17\)–\(19\)](#), we used three simple properties: $\|A\|_F^2 = \text{tr}(AA^H)$, $B^H = B$, and $B^2 = B$.

Appendix B. An SVD-based estimator

We have the claim

$$\hat{T}_{2,svd} = \arg \min_{T_2} \sum_{k=1}^N \|Y_k - au_1 \exp(-2\tau_k/T_2)\|^2 \quad (23)$$

$$= \operatorname{argmin}_{T_2} \sum_{k=1}^N \|v_1 - ab(T_2)\|^2. \quad (24)$$

This equality in (24) is demonstrated using simple properties of the trace operator, tr , and completing the square. Define b_θ to be any length N vector parametrized by θ , and let $Y = U SV^H$ be the singular value decomposition of the noisy data array, Y . Recall that $\|A\|_F^2 = \text{tr}(A^H A)$ and columns of U are orthonormal to learn

$$\begin{aligned}\hat{\theta}_{svd} &= \underset{\theta}{\operatorname{argmin}} \left\| Y - au_1 b_\theta^H \right\|_F^2 \\ &= \underset{\theta}{\operatorname{argmin}} \text{tr} \left\{ (VSU^H - ab_\theta u_1^H) (USV^H - au_1 b_\theta^H) \right\} \\ &= \underset{\theta}{\operatorname{argmin}} \text{tr} \left\{ VSU^H USV^H - 2ab_\theta \sigma_1 v_1^H + a^2 b_\theta u_1^H u_1 b_\theta \right\} \\ &= \underset{\theta}{\operatorname{argmin}} \sum_{k=1}^N \sigma_k^2 - \text{tr} \left\{ 2ab_\theta \sigma_1 v_1^H \right\} + \text{tr} \left\{ a^2 b_\theta b_\theta^H \right\} \\ &= \underset{\theta}{\operatorname{argmin}} s \sum_{k=2}^N \sigma_k^2 + \|\sigma_1 v_1 - ab_\theta\|^2 \\ &= \underset{\theta}{\operatorname{argmin}} \|\sigma_1 v_1 - ab_\theta\|^2.\end{aligned}$$

which establishes that which was to be shown. Further, following again the steps in Appendix A, we have the equivalent representation,

$$\hat{\theta}_{svd} = \underset{\theta}{\operatorname{argmin}} \frac{b_\theta^H v_1 v_1^H b_\theta}{b_\theta^H b_\theta}. \quad (25)$$

The effectiveness of the suboptimal estimator in (25) can be illuminated by comparison to the MLE. To this end,

$$\begin{aligned}\hat{\theta}_{ml} &= \underset{\theta}{\operatorname{argmin}} \frac{b_\theta^H Y^H Y b_\theta}{b_\theta^H b_\theta} = \underset{\theta}{\operatorname{argmin}} \frac{b_\theta^H V S^2 V^H b_\theta}{b_\theta^H b_\theta} \\ &= \underset{\theta}{\operatorname{argmin}} \frac{b_\theta^H v_1 v_1^H b_\theta}{b_\theta^H b_\theta} + \frac{1}{b_\theta^H b_\theta} \sum_{k=2}^N \left(\frac{\sigma_k}{\sigma_1} \right)^2 |b_\theta^H v_k|^2.\end{aligned} \quad (26)$$

Thus, the first term in the cost function (26) is identical to the cost in the SVD-based estimator. The second term is absent from the SVD estimator, which is therefore suboptimal. However, the role of the second term is made minor in two ways. First, the ratio of squared singular values greatly reduces the influence of the second term; second, the v_k 's are orthogonal, leaving the inner product $b_\theta^H v_k$ having small magnitude for $k > 1$.

References

- [1] S.S. Eaton, G.R. Eaton, L.J. Berliner (Eds.), Biomedical EPR, Part A: Free Radicals, Metals, Medicine and Physiology, Kluwer Academic, New York, 2004.
- [2] S. Matsumoto, H. Yasui, J.B. Mitchell, M.C. Krishna, Imaging cycling tumor hypoxia, *Cancer Res.* 70 (24) (2010) 10019–10023.
- [3] D.S. Vikram, J.L. Zweier, P. Kuppusamy, Methods for noninvasive imaging of tissue hypoxia, *Antioxid. Redox Signaling* 9 (10) (2007) 1745–1756.
- [4] R. Ahmad, P. Kuppusamy, Theory, instrumentation, and applications of electron paramagnetic resonance oximetry, *Chem. Rev.* 110 (5) (2010) 3212–3236.
- [5] B. Epel, S.V. Sundaramoorthy, E.D. Barth, C. Mailer, H.J. Halpern, Comparison of 250 MHz electron spin echo and continuous wave oxygen EPR imaging methods for in vivo applications, *Med. Phys.* 38 (4) (2011) 2045–2052.
- [6] M. Bowman, T. Michalski, M. Peric, H. Halpern, et al., Fourier-transform-EPR and low-frequency-EPR studies of nitroxides, *Pure Appl. Chem.* 62 (2) (1990) 271–274.
- [7] C. Mailer, S.V. Sundaramoorthy, C.A. Pelizzari, H.J. Halpern, Spin echo spectroscopic electron paramagnetic resonance imaging, *Magn. Reson. Med.* 55 (4) (2006) 904–912.
- [8] S. Subramanian, N. Devasahayam, S. Matsumoto, K. Saito, J.B. Mitchell, M.C. Krishna, Echo-based single point imaging (ESPI): a novel pulsed EPR imaging modality for high spatial resolution and quantitative oximetry, *J. Magn. Reson.* 218 (2012) 105–114.
- [9] S. Subramanian, M.C. Krishna, Dancing with the electrons: time-domain and CW in vivo EPR imaging, *Magn. Reson. Insights* 24 (2) (2012) 43–47.
- [10] E.L. Hahn, Spin echoes, *Phys. Rev.* 80 (4) (1950) 580.
- [11] M. Tseitin, R.W. Quine, G.A. Rinard, S.S. Eaton, G.R. Eaton, Digital EPR with an arbitrary waveform generator and direct detection at the carrier frequency, *J. Magn. Reson.* 213 (1) (2011) 119–125.
- [12] M.K. Bowman, M.D. Krzyaniak, A.A. Cruce, R.T. Weber, Skew projection of echo-detected EPR spectra for increased sensitivity and resolution, *J. Magn. Reson.* 231 (2013) 117–125.
- [13] L.C. Potter, J.N. Ash, SpinEchoMLE.m, Matlab Central File Exchange, 2013. <<http://www.mathworks.com/matlabcentral/fileexchange/>>.
- [14] G. Golub, C. Van Loan, *Matrix Computations*, Johns Hopkins University Press, Baltimore, 1989.
- [15] G. He, R.A. Shankar, M. Chzhan, A. Samoilov, P. Kuppusamy, J.L. Zweier, Noninvasive measurement of anatomic structure and intraluminal oxygenation in the gastrointestinal tract of living mice with spatial and spectral epr imaging, *Proc. Natl. Acad. Sci.* 96 (8) (1999) 4586–4591.
- [16] H. Van Trees, *Detection, Estimation, and Modulation Theory: Part I*, Wiley, New York, 1968.
- [17] H.V. Poor, *An Introduction of Signal Detection and Estimation*, second ed., Springer, 1994.
- [18] Y. Talmor, L. Shtirberg, W. Harneit, O.Y. Rogozhnikova, V. Tormyshev, A. Blank, Molecular diffusion in porous media by PGSE ESR, *Phys. Chem. Chem. Phys.* 12 (23) (2010) 5998–6007.
- [19] L. Shtirberg, Y. Twig, E. Dikarov, R. Halevy, M. Levit, A. Blank, High-sensitivity Q-band electron spin resonance imaging system with submicron resolution, *Rev. Sci. Instrum.* 82 (4) (2011) 043708.
- [20] J. Palmer, L. Potter, R. Ahmad, Optimization of magnetic field sweep and field modulation amplitude for continuous-wave EPR oximetry, *J. Magn. Reson.* 209 (2) (2011) 337–340.
- [21] B. Epel, H.J. Howard, Comparison of transverse and spin-lattice relaxation based electron paramagnetic resonance oxygen images, in: *Biomedical Imaging: From Nano to Macro*, 2011 IEEE International Symposium, Chicago, IL, 2011, pp. 754–757.
- [22] J.-M. Bonny, M. Zanca, J.-Y. Boire, A. Veyre, T2 maximum likelihood estimation from multiple spin-echo magnitude images, *Magn. Reson. Med.* 36 (2) (1996) 287–293.
- [23] S.J. Graham, P.L. Stanchev, M.J. Bronskill, Criteria for analysis of multicomponent tissue T2 relaxation data, *Magn. Reson. Med.* 35 (3) (1996) 370–378.
- [24] J.G. Raya, O. Dietrich, A. Horng, J. Weber, M.F. Reiser, C. Glaser, T2 measurement in articular cartilage: impact of the fitting method on accuracy and precision at low SNR, *Magn. Reson. Med.* 63 (1) (2010) 181–193.
- [25] M. Bydder, J. Du, Noise reduction in multiple-echo data sets using singular value decomposition, *Magn. Reson. Imaging* 24 (7) (2006) 849–856.
- [26] H. Barkhuijsen, R. de Beer, D. van Ormondt, Error theory for time-domain signal analysis with linear prediction and singular value decomposition, *J. Magn. Reson.* 67 (2) (1986) 371–375.
- [27] G. Redler, B. Epel, H.J. Halpern, Principal component analysis enhances SNR for dynamic electron paramagnetic resonance oxygen imaging of cycling hypoxia in vivo, *Magn. Reson. Med.* <http://dx.doi.org/10.1002/mrm.24631>.